

Visual-Inertial Navigation with Feature Confidence Analysis

 ISSN 1751-8644
 doi: 0000000000
 www.ietdl.org

Chang-Ryeol Lee, Kuk-Jin Yoon ✉

School of Electrical Engineering and Computer Science, Gwangju Institute of Science and Technology (GIST), 123 Cheomdangwagi-ro, Buk-gu, Gwangju, Korea

✉ E-mail: kjyoon@gist.ac.kr

Abstract: Visual-Inertial Odometry (VIO) utilizes an Inertial Measurement Unit (IMU) to overcome the limitations of Visual Odometry (VO). However, the VIO for vehicles in large-scale outdoor environments still has some difficulties in estimating forward motion with distant features. To solve these difficulties, we propose a robust VIO method based on the analysis of feature confidence in forward motion estimation using an IMU. We first formulate the VIO problem by using effective trifocal tensor geometry. Then, we infer the feature confidence by using the motion information obtained from an IMU and incorporate the confidence into the Bayesian estimation framework. Experimental results on the public KITTI dataset show that the proposed VIO outperforms the baseline VIO, and it also demonstrates the effectiveness of the proposed feature confidence analysis and confidence-incorporated ego-motion estimation framework.

1 Introduction

Odometry, which estimates 6-DOF ego-motion, is a crucial technology for mobile applications. In robotics and computer vision community, Visual Odometry (VO) using cameras has been extensively studied for robot navigation [1] and autonomous driving [2] for decades. Practically, VO has great advantages in GPS-denied environments such as urban, military, underwater, and indoor areas, and provides less drifted results compared to Wheel Odometry (WO) and Inertial Odometry (IO). However, it also has some limitations: it cannot estimate the absolute scale of ego-motion and its performance highly depends on the scene and/or surrounding environments.

For these reasons, Inertial Measurement Units (IMUs) have been utilized for VO, named Visual-Inertial Odometry (VIO), and led outstanding advances in ego-motion estimation [3]. The VIO exploits the inertial measurements as well as a camera to get the scale information and accurate rotation estimates. It shows more robust performance to variations of scene conditions (*e.g.* illumination, weather, texture, etc.) than VO thanks to the complementary properties of heterogeneous sensors [4].

However, despite the aid of an IMU, these vision-based odometry methods for vehicles in large-scale outdoor environments still have some difficulties in estimating forward motion with distant features, where accurate estimation of the forward motion is a crucial issue because vehicles (*i.e.* cameras) move mostly forward. When they move forward and only distant features are available in the scene, it causes the lack of observation for translational motion estimation. For example, feature points located along the optical axis do not have any displacements in the images when a camera moves along the optical axis. In this sense, *features near the motion axis are not informative for forward motion estimation*. Furthermore, distant features have small displacements under translational camera motion. Actually, it is a well-known fact that *distant features are not informative for translation motion estimation* [5]. Consequently, *distant features along the motion direction* have vast uncertainty for forward motion estimation due to the aforementioned reasons. Ironically, however, such uncertain features are easy to track in the image sequence because of the projectivity of an image and their small displacement under translation as shown in Fig. 1.



Fig. 1: Some outdoor images from the KITTI vehicle sequences and extracted local features. Many feature points are located near the motion axis and distant in the scene. Such distant feature points near the motion axis have large uncertainty for forward motion estimation.

Yang *et al.*[6] analyzed the uncertainty of a 3D feature point, U_p , during forward motion for scene reconstruction from motion as

$$U_p = \frac{\sigma}{t_3 R} \sqrt{\frac{N}{X^2 + Y^2}}, \quad N = f(X, Y, Z), \quad (1)$$

where σ is the standard deviation of measurement noise, R is the distance of a 3D feature point, t_3 is the forward translation of a camera, and (X, Y, Z) is a 3D location of a feature point. Here, a composition function f is dominated by Z^8 , and this indicates that the uncertainty of the measurement increases as the depth of a feature point increases. In addition, we can see that feature points around the motion axis have large uncertainty because X, Y, R are placed in the denominator.

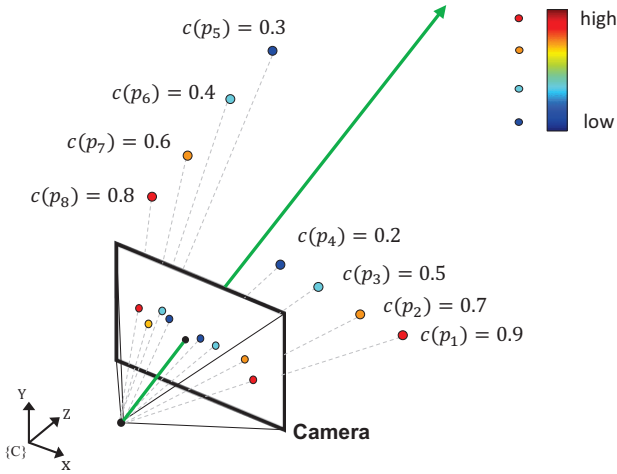


Fig. 2: Concept of a confidence map during forward motion. As the depth (Z-axis) of the feature increases, the confidence of the feature decreases. In addition, as the distance of the feature from the motion direction increases, the confidence of the feature increases.

Our work was inspired by this simple analysis on the uncertainty of measurements. In this paper, we define the confidence of a feature point in motion estimation as the opposite concept of uncertainty due to their inverse correlation. Fig. 2 shows the concept of the feature confidence when a camera moves forward. We present a robust VIO method in a moving platform by analyzing the confidence of features during forward motion. The cue for the confidence is the motion direction obtained from inertial measurements, and it is incorporated into measurement noise covariance in the Bayesian estimation framework. Our confidence analysis can be easily utilized for existing vision-based odometry frameworks for vehicles with inertial measurements or pre-estimated motion from images.

The main contributions of the paper can be summarized as follows:

- Analysis of feature confidence in forward motion estimation based on inertial measurements, and
- Confidence-incorporated Bayesian ego-motion estimation framework.

This paper is organized as follows. We review related works in Section 2 and describe the system configuration and notations in Section 3. Then, we briefly summarize the baseline VIO framework [4] in Section 4. We describe how the confidence of features can be inferred and incorporated into our framework in Section 5, and illustrate experimental results in Section 6. Finally, we discuss the limitation and future works and conclude the paper in Section 7.

2 Related Works

We review VIO methods and feature handling methods for vision-based odometry.

Visual-Inertial Odometry. In the early stage, inertial measurements were used for structure-from-motion applications [7–9]. Those methods simply integrated inertial measurement data into the Bayesian estimation framework to predict ego-motion. Then, the fusion of visual and inertial measurement data has been theoretically validated and various state estimation techniques have been also applied [10–13]. These methods usually require heavy computational power because of the estimation of 3D landmarks. As a result, a real-time issue on VIO has become important, and many efficient algorithms have been studied [14, 15].

Nowadays, the inertial measurements are more effectively used in various ways for many applications. For example, the inertial data were used to solve an inverse depth problem in SLAM [16]. Also, researches to estimate the scale of camera motion by using

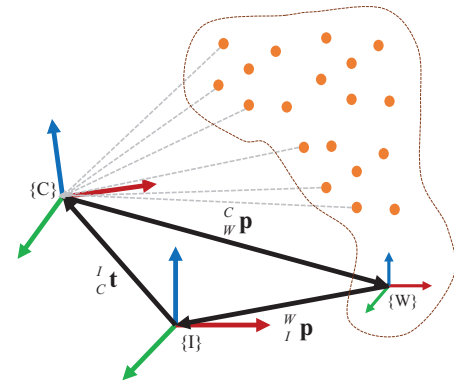


Fig. 3: Relation between 3D feature points in world coordinates and rigidly connected IMU-camera coordinates. Orange dots indicate feature points in world coordinates. Dashed gray arrows represent the projection of the features to camera coordinates.

inertial data were studied [11, 17, 18]. In some works, the calibration of IMUs and between an IMU and a camera, which directly affects on estimation performance, was estimated together with the motion [9, 19, 20]. Feature characteristics was often exploited as constraints for estimation [21, 22], and there was some efforts to resolve issues arisen in smart-phones [20, 23]. Recently, sliding-window approaches have been proposed for VIO [4, 24, 25], and optimization-based VIO methods have been also studied [26, 27].

Feature Handling for Odometry. Kaess *et al.*[5] proposed the separated estimation of rotation and translation to handle degenerate cases where features are not distributed evenly. They used depth cue based on stereo cameras. Badino *et al.*[28] pointed out that handling the noise of feature measurement is an important issue and tried to suppress the noises of features by integrating features in multiple frames. On the other hand, Song *et al.*[29] used a learning technique to resolve the different uncertainties of multiple cues. Recently, Zhang and Vela proposed to select important features for ego-motion estimation [30]. This is the most similar work to ours. However, unlike Zhang’s algorithm, we exploit simple confidence analysis based on inertial measurements instead of complex observability measure.

3 System Configuration and Notations

Before presenting the problem formulation and the proposed algorithm, we describe the system configuration and some notations to make our formulation clearer. Our system consists of a single IMU and a single camera. They are rigidly connected and, therefore, the transformation between their coordinates can be described by 3-DOF rotation and 3-DOF translation. Fig. 3 shows the relation between 3D feature points in the world coordinate and rigidly connected IMU-camera coordinates. $\{I\}$ denotes the IMU coordinate, and $\{W\}$ represents the world coordinate. Special subscripts (*i.e.*, W , I and C) explain the reference coordinate explicitly. For example, when \mathbf{p} denotes the 3D position, $^W \mathbf{p}$ represents the IMU 3D position with respect to the world coordinate $\{W\}$; here, the subscript I represents an IMU. When \mathbf{t} denotes 3D translation, $^I \mathbf{t}$ represents camera translation with respect to the IMU coordinate $\{I\}$; here, the subscript C represents a camera.

4 Visual Inertial Odometry

In the ego-motion estimation problem, 3D landmarks are commonly estimated together with the 6D motion vector. This approach requires a large amount of computational power proportional to the number of landmarks in general. For efficient and accurate ego-motion estimation, our work is based on the sliding window

strategy that uses consecutive frames without estimating any 3D landmarks. We exploit trifocal-tensor-based VIO [4] as a baseline odometry algorithm with little modifications. In this section, we briefly summarize the baseline algorithm.

Basically, we estimate the state \mathbf{x} in (2) by using the measurement \mathbf{z} in (10) with the Unscented Kalman Filter (UKF) because both the state transition and measurement models are nonlinear. The state comprises 3D poses of an IMU in three consecutive frames for trifocal tensor geometry and biases of inertial measurements:

$$\mathbf{x} = \left[\begin{matrix} {}^W_I \mathbf{p}_1^\top & {}^W_I \mathbf{v}^\top & {}^W_I \mathbf{q}_1^\top & \mathbf{b}_a^\top & \mathbf{b}_g^\top & {}^W_I \mathbf{p}_2^\top & {}^W_I \mathbf{q}_2^\top & {}^W_I \mathbf{p}_3^\top & {}^W_I \mathbf{q}_3^\top \end{matrix} \right]^\top, \quad (2)$$

where ${}^W_I \mathbf{q}_i \in \mathfrak{R}^4$ is a unit quaternion representing the orientation, ${}^W_I \mathbf{p}_i \in \mathfrak{R}^3$ is the position, and the subscript i ($i \in \{1, 2, 3\}$) denotes the index of the poses in order of time (*i.e.*, ${}^W_I \mathbf{q}_1$ and ${}^W_I \mathbf{p}_1$ are the foremost pose). ${}^W_I \mathbf{v} \in \mathfrak{R}^3$ is the velocity, and $\mathbf{b}_a \in \mathfrak{R}^3$ is the bias of acceleration measurements, and $\mathbf{b}_g \in \mathfrak{R}^3$ is the bias of gyroscope measurements, respectively.

4.1 Transition model

Based on the defined state vector, the state transition is formulated as

$$\mathbf{x}_{k+1} = f(\mathbf{x}_k) + \mathbf{w}_k = \begin{bmatrix} f_{pose}(\mathbf{x}_k^{[1:23]}, \mathbf{u}_k) \\ f_{bias}(\mathbf{x}_k^{[11:16]}) \end{bmatrix} + \mathbf{w}_k, \quad (3)$$

where superscript of \mathbf{x} denotes the indexes of elements in the state vector, and the modeling noise $\mathbf{w}_k \in \mathfrak{R}^{30}$ is assumed to be the white Gaussian noise as $\mathbf{w}_k \sim \mathcal{N}(\mathbf{0}, \mathbf{Q})$ where $\mathbf{Q} \in \mathfrak{R}^{30 \times 30}$, and $\mathbf{u}_k \in \mathfrak{R}^6$ is a control input obtained from the IMU.

The pose state transition model in (3) is formulated based on the basic law of the uniformly accelerated motion [31] as

$$\begin{aligned} \mathbf{x}_{k+1}^{[1:16]} &= f_{pose}(\mathbf{x}_k^{[1:16]}) = \begin{bmatrix} {}^W_I \mathbf{p}_{1,k+1} \\ {}^W_I \mathbf{v}_{k+1} \\ {}^W_I \mathbf{q}_{1,k+1} \end{bmatrix} \\ &= \begin{bmatrix} {}^W_I \mathbf{p}_{1,k} + {}^W_I \mathbf{v}_k \Delta T + {}^W \mathbf{a}_k \frac{\Delta T^2}{2} \\ {}^W_I \mathbf{v}_k + {}^W \mathbf{a}_k \Delta T \\ e^{-I \mathbf{g}_k \frac{\Delta T}{2}} \odot {}^W_I \mathbf{q}_{1,k} \end{bmatrix}, \end{aligned} \quad (4)$$

where the operator \odot denotes the quaternion product. To predict the next position ${}^W_I \mathbf{p}_{k+1}$ and orientation ${}^W_I \mathbf{q}_{k+1}$ of an IMU, we use the acceleration ${}^W \mathbf{a}$ and the angular velocity ${}^W \mathbf{w}$ during some time interval. They are obtained from the inverse process of generating inertial measurements [32] as

$$\begin{bmatrix} {}^W_I \mathbf{a}_k \\ {}^W_I \mathbf{g}_k \end{bmatrix} = \begin{bmatrix} \mathbb{R}({}^W_I \mathbf{q}_k) [\mathbf{a}_{m,k} - \mathbf{b}_{a,k} - \mathbf{w}_a] + {}^W \mathbf{g} \\ \mathbf{g}_{m,k} - \mathbf{b}_{g,k} - \mathbf{w}_g \end{bmatrix}, \quad (5)$$

where \mathbf{w}_a and \mathbf{w}_g are acceleration and gyroscope measurement noises, respectively, and assumed to be white Gaussian noise, $\{\mathbf{a}_{m,k}, \mathbf{g}_{m,k}\} \subset \mathbf{u}_k$ are the measurements from the IMU. The matrix $\mathbb{R}(\cdot)$ denotes a direct cosine matrix converted from the unit-quaternion \mathbf{q} . Then, the second and third poses are transited by the first pose and second poses in the previous time instance.

$$\begin{bmatrix} {}^W_I \mathbf{p}_{2,k+1} \\ {}^W_I \mathbf{q}_{2,k+1} \\ {}^W_I \mathbf{p}_{3,k+1} \\ {}^W_I \mathbf{q}_{3,k+1} \end{bmatrix} = \begin{bmatrix} {}^W_I \mathbf{p}_{1,k} \\ {}^W_I \mathbf{q}_{1,k} \\ {}^W_I \mathbf{p}_{2,k} \\ {}^W_I \mathbf{q}_{2,k} \end{bmatrix} \quad (6)$$

The bias state transition model in (3) is formulated by Brownian motion as $\mathbf{x}_{k+1}^{[11:16]} = f_{bias}(\mathbf{x}_k^{[11:16]})$.

Algorithm 1 Unscented Kalman Filter (UKF) with Feature Confidence Analysis

• Initialization at $k = 0$

$$\hat{\mathbf{x}}_0 = E[\mathbf{x}_0], \mathbf{P}_0 = E[(\mathbf{x}_0 - \hat{\mathbf{x}}_0)(\mathbf{x}_0 - \hat{\mathbf{x}}_0)^\top]$$

• State Estimation with Confidence Analysis, $k \geq 0$

(1) Prediction

$$[\hat{\mathbf{x}}_{k+1}^-, \mathbf{P}_{k+1}^-] = \text{UKF_PREDICT}(\hat{\mathbf{x}}_k^+, \mathbf{P}_k^+, \mathbf{Q}_k, f, \mathbf{u}_k)$$

(2) 3-points RANSAC with predicted states

$$\mathbf{z}_{k+1}^{inlier} = \text{RANSAC}(\mathbf{z}_{k+1}, \hat{\mathbf{x}}_{k+1}^-, \theta)$$

(3) Confidence inference in Section 5.2

$$\mathbf{C}_{z,k+1} = \text{INFER}(\mathbf{u}_k, \mathbf{z}_{k+1}^{inlier})$$

(4) Update with confidence in Section 5.3

$$[\hat{\mathbf{x}}_{k+1}^+, \mathbf{P}_{k+1}^+] = \text{UKF_UPDATE}(\hat{\mathbf{x}}_{k+1}^-, \mathbf{P}_{k+1}^-, h, \mathbf{z}_{k+1}^{inlier}, \mathbf{C}_{z,k+1})$$

▷ f is a transition model in Section 4.1.

▷ h is a measurement model in Section 4.2.

▷ \mathbf{u}_k is a control input, \mathbf{z}_k is a measurement.

▷ θ is a threshold for RANSAC.

4.2 Measurement model

As measurements for state estimation, feature points extracted from images are used with trifocal tensor geometry. The trifocal tensor encodes the geometric relationship between scene structure and three images that capture the scene at different viewpoints. From a line and the corresponding two points in 3D space and three projection matrices of each image, the trifocal tensor $\mathbf{T} \in \mathfrak{R}^{3 \times 3 \times 3}$ is given by

$$\mathbf{T}_j = \mathbf{P}_{1,4} (\mathbf{P}_{2,j})^\top - \mathbf{P}_{2,4} (\mathbf{P}_{1,j})^\top, \quad (7)$$

where subscript $j \in \{1, 2, 3\}$ denotes the column index of a matrix or a trifocal tensor, and $\mathbf{P}_i \in \mathfrak{R}^{3 \times 4}$, $i \in \{1, 2, 3\}$, are camera projection matrices of three consecutive frames. For example, $\mathbf{P}_{i,j}$ is the j -th column vector of the i -th camera projection matrix. The projection matrices of cameras are acquired from the IMU pose states of (3) and transformation parameters ${}^I_C \mathbf{t}$, ${}^I_C \mathbf{Q}$ between an IMU and a camera.

A point in the first image can be predicted from the corresponding line in the second image and the corresponding point in the third image with the trifocal tensor. It is called point-line-point correspondence in literature given as

$$\mathbf{f}_1 = \mathbf{K} \left(\sum_j (\mathbf{f}_{3,j}) \mathbf{T}_j^\top \right) \mathbf{l}_2, \quad (8)$$

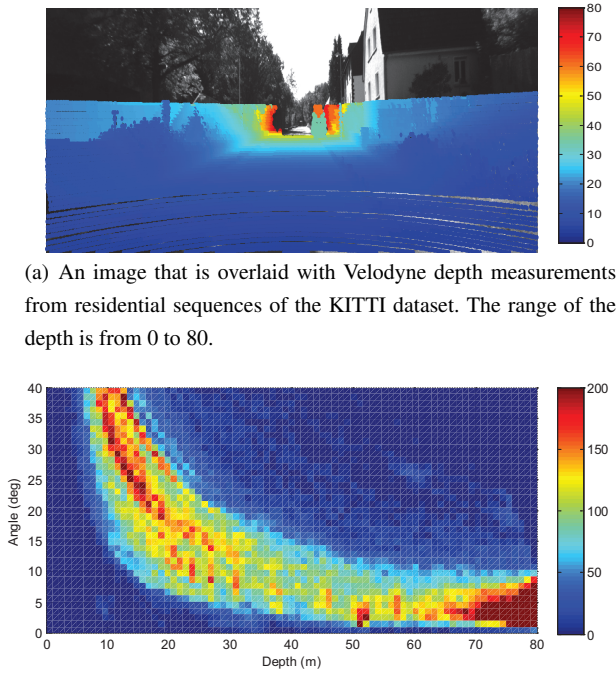
where $\mathbf{f}_i \in \mathfrak{R}^3$, $\mathbf{l}_i \in \mathfrak{R}^3$ are a 3D point vector and a line vector in i -th camera coordinates, respectively. $\mathbf{f}_{i,j}$ is the j -th element of a 3D point vector in the i -th camera, and \mathbf{K} is an intrinsic parameter matrix of a camera.

A measurement $\mathbf{z}_m \in \mathfrak{R}^2$, $m \in \{1, \dots, M\}$ in the first image is stacked to construct the measurement vector \mathbf{z} for motion estimation as $\mathbf{z} = [\mathbf{z}_1^\top, \dots, \mathbf{z}_M^\top]^\top$. The measurement model h_m is defined as

$$\mathbf{z}_m = \begin{bmatrix} u_m \\ v_m \end{bmatrix}, \quad (9)$$

$$\begin{bmatrix} u_m \\ v_m \\ 1 \end{bmatrix} = h_m(\mathbf{x}; \mathbf{f}_3^m, \mathbf{l}_2^m) + \mathbf{v}_m = \mathbf{K} \left(\sum_i (\mathbf{f}_{3,i}^m) \mathbf{T}_j^\top \right) \mathbf{l}_2 + \mathbf{v}_m, \quad (10)$$

where measurement noise $\mathbf{v} \in \mathfrak{R}^{2M}$ is assumed to be white Gaussian noise as $\mathbf{v} \sim \mathcal{N}(\mathbf{0}, \mathbf{R})$.



(a) An image that is overlaid with Velodyne depth measurements from residential sequences of the KITTI dataset. The range of the depth is from 0 to 80.

(b) The 2D histogram of the depth and the angle of features. The angle is defined with the 3D position vector and the motion axis. (Total 135,671 features points from the 16 sequences of the KITTI residential dataset are counted for the statistics.)

Fig. 4: The 2D histogram of the depth and the angles of features from the 16 sequences of the KITTI residential dataset

5 Confidence-incorporated Kalman Filter

In this section, we illustrate our main contributions, the analysis of feature confidence in forward motion estimation and the confidence-incorporated Bayesian ego-motion estimation framework. We exploit depth cues with the street assumption and motion cues from inertial measurements for confidence analysis. With these cues, our confidence inference algorithm can be applicable to efficient VIO methods which do not explicitly estimate depth as states. Algorithm 1 shows the overall framework of the proposed confidence-incorporated estimation algorithm. Unlike [4], we use 3-point RANSAC for robustness instead of 1-point RANSAC.

5.1 Street Assumption

We assume the general moving vehicle platform in street environments. Motions of a vehicle are mainly composed of forward and rotation (pitch and yaw) motions. During forward motion, the static feature points, which are inliers for ego-motion estimation, are extracted from trees, houses (or buildings), and cars along the street. As a result, the distant feature points are placed in the middle part of the image as shown in Fig. 4(a). We statistically analyzed the relationship between the depth of the features and the motion axis for forward motion by the 16 residential sequences of the public KITTI dataset. According to our analysis, almost all features are located along the motion axis. So, we can conclude that the depth of features and the angles between the motion axis and the 3D position vectors of features are inversely proportional. Fig. 4(b) strongly supports our arguments on street assumption. This shows that the depth of a feature can be roughly inferred from its angle with the motion axis. The geometric definitions of the angle and the depth of a feature and their relation are described in Fig. 5. We exploit this observation to infer the confidence of feature points.

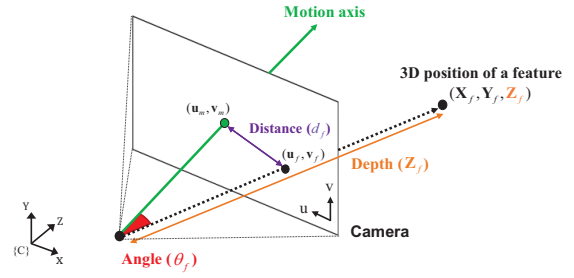


Fig. 5: Relation of the motion axis vector and the 3D position vector of a feature. θ_f is the angle between the motion axis and the 3D position of a feature. d_f is the distance between (u_f, v_f) and (u_m, v_m) in the image coordinate. Z_f is the depth of a feature.

5.2 Inference of feature confidence

As we illustrated in Section 1, distant feature points located along the motion direction have low confidence for estimating forward motion. With this intuition, we infer the confidence of all features in an image. We exploit the angle information between the motion axis and the 3D position vector of a feature point mentioned in Sec 5.1. The angle implicitly includes the depth information in the 3D camera coordinates under the aforementioned street assumption, as well as the distance information between the motion axis and a feature in the 2D image coordinate as described in Fig. 5. For example, if the depth of a feature increases, then the angle of the feature decreases. If the distance of a feature to the motion axis decreases, then the angle of the feature decreases. That is, the angle of a feature to the motion axis is proportional to the confidence of a feature for estimating forward motion.

From this analysis, we define the feature confidence for forward motion estimation based on the motion direction as

$$c_{t,m} = \cos^{-1} \left(\frac{C_{\mathbf{v}} \cdot \mathbf{f}_1^m}{\|C_{\mathbf{v}}\| \|\mathbf{f}_1^m\|} \right), \quad (11)$$

where $\|\cdot\|$ denotes the magnitude of a vector, $C_{\mathbf{f}_1^m} \in \mathfrak{R}^3$ is the 3D position vector of the m -th feature in the first camera coordinate among three consecutive camera coordinates in Sec 4.2, and $C_{\mathbf{v}}^T \in \mathfrak{R}^3$ is a velocity of the camera coordinate. Fig. 6 shows feature points with the confidence map inferred by the motion direction for the forward motion estimation.

However, the matching confidence of feature points is usually opposite to the confidence for estimating forward motion. For example, the matching accuracy of distant features are generally higher than that of close features, because the displacements of distant features are small in forward motion. Although it looks like a paradox on feature confidence, we believe that the RANSAC process guarantees the measurement noise of features to be small and consistent.

The inferred feature confidence is only applicable for forward motion. For this reason, we need to examine the ratio of forward and rotation motions in a vehicle motion by inertial measurement analysis. We define the forward motion ratio τ as

$$\tau = \frac{\|W_I \mathbf{v}\|}{\|\mathbf{g}_m\| + \|W_I \mathbf{v}\|}, \quad (12)$$

where \mathbf{a}_m is acceleration measurements and \mathbf{g}_m is gyroscope measurements. Even though the units of acceleration and angular velocity are different, the motion ratio τ is empirically acceptable, because the magnitudes of two measurements are proportional to the translational and rotational force. The scale problem caused from different units can be resolved by leaning-based regression techniques. Fig. 7 shows motion changes with time and corresponding τ values obtained by the inertial measurement analysis.



Fig. 6: Feature points with a confidence map inferred from the motion direction (brighter pixels in the confidence map represent larger confidence).

Final confidence of a feature is determined as

$$c_m = \tau c_{t,m}. \quad (13)$$

5.3 Update with confidence

The Kalman filter considers the uncertainties of a system and measurements to handle various system configurations and measurement noise. Under normal circumstances, the uncertainties are modeled as common white Gaussian noise because it makes the system easy to solve. In the case of image features, all features are assumed to have the same uncertainty in general as

$$\mathbf{z} = h(\mathbf{x}) + \mathbf{v}, \quad p(\mathbf{v}) \sim \mathcal{N}(\mathbf{0}, \mathbf{R}). \quad (14)$$

However, in our framework, we impose different uncertainties to measurement noise covariance \mathbf{R} based on the feature confidence analysis. The feature confidences described in Sec. 5.2 are block-diagonalized as

$$\mathbf{C}_f = \text{bl_diag}(c_1 \mathbf{I}_2, \dots, c_M \mathbf{I}_2). \quad (15)$$

Then, the confidence matrix \mathbf{C}_f is multiplied to \mathbf{R} . As a result, the Kalman gain \mathbf{K}_c reflecting the feature confidence is produced as follows.

$$\mathbf{K}_c = \mathbf{P}_{xy}(\mathbf{P}_{yy} + \mathbf{C}_f \mathbf{R})^{-1} \quad (16)$$

Here \mathbf{P}_{xy} is state-measurement cross covariance and \mathbf{P}_{yy} is measurement covariance for UKF Kalman gain.

This Kalman gain is used to update state \mathbf{x}^- and state error covariance \mathbf{P}^- as follows.

$$\hat{\mathbf{x}}^+ = \hat{\mathbf{x}}^- + \mathbf{K}_c(\mathbf{z} - \hat{\mathbf{z}}) \quad (17)$$

$$\mathbf{P}^+ = \mathbf{P}^- - \mathbf{K}_c \mathbf{P} \mathbf{K}_c^\top \quad (18)$$

6 Experimental Results

We performed experiments on public KITTI datasets [2]. However, since the odometry benchmark datasets on the KITTI website do not provide inertial measurements for VIO, we utilized KITTI raw data datasets which include all information for VIO. We evaluated our algorithm on 16 sequences in residential environments longer than 100 (m). Residential sequence* is the most proper sequence

*http://www.cvlibs.net/datasets/kitti/raw_data.php?type=residential

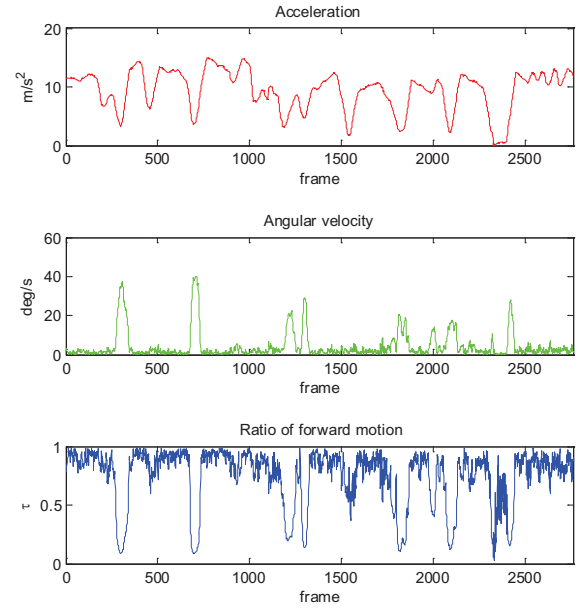


Fig. 7: Motion analysis results of the sequence 2011_09_30_drive_0018 (#10 in Sec 6) using inertial measurements (upper: acceleration measurements, middle: gyroscope measurements, lower: forward motion ratio).

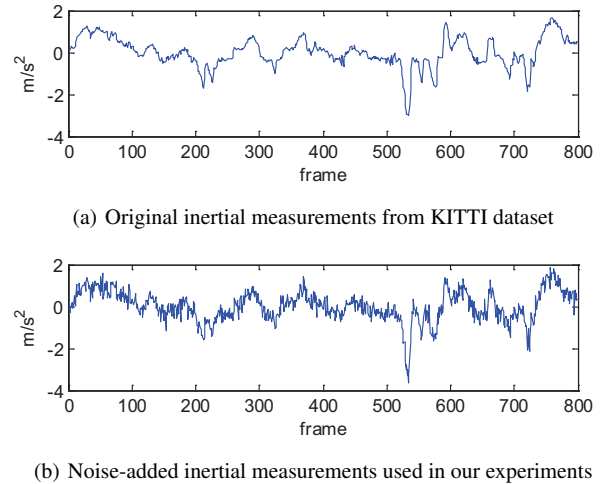


Fig. 8: Comparison of inertial measurements. Y-axis denotes the acceleration.

compared to City, Road, and Campus sequences because they have small numbers of moving objects.

However, the inertial measurements provided from the KITTI datasets are highly accurate so that they can be used as ground truth for evaluation. On the other hand, it is well-known that IMU uncertainty is severely high. We assume general environments that use a less accurate low-cost IMU and camera. Therefore, it is not suitable to use the inertial measurements from the KITTI dataset directly as inputs of the baseline and the proposed VIO. For this reason, we added Gaussian noise of the low-cost IMU ($\sigma_{n_a} = 0.25 \text{ m/s}^2$, $\sigma_{n_g} = 0.26^\circ/\text{s}$) to inertial measurements of KITTI datasets. The noise strength was determined from the real data by using the technique described in [33]. Fig. 8 shows the original inertial measurements of the KITTI dataset and the noisy input used in our experiments. Image features used for motion estimation were extracted and matched by using the SIFT descriptor which is a well-known robust descriptor.

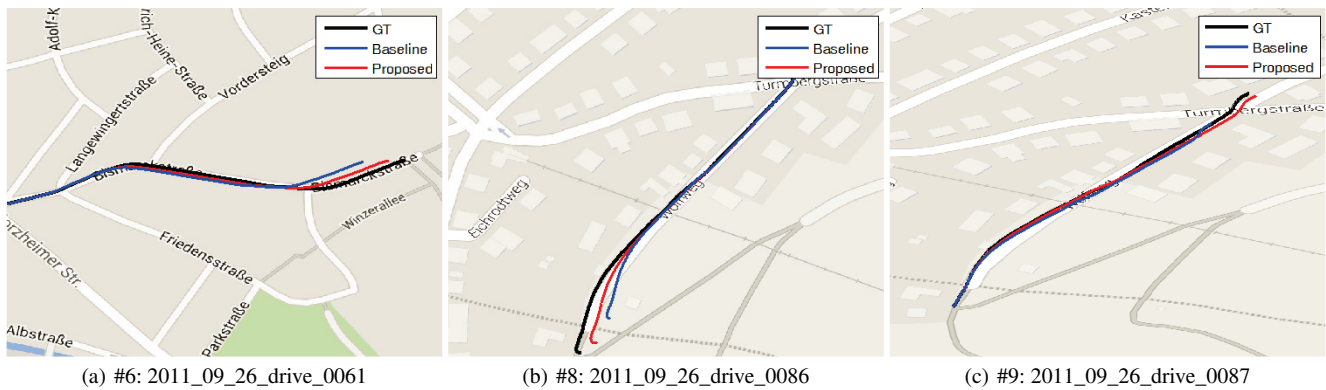


Fig. 9: Selective qualitative comparison results between the baseline and the proposed algorithm.

For fair evaluation, we adopt evaluation metrics and codes from the KITTI benchmark[†].

We exploited the Hu's work as the baseline odometry [4]. However, the proposed confidence analysis can be incorporated into any Bayesian estimation framework as we already mentioned in Section 1. All parameters for baseline and proposed VIO such as initial error covariance \mathbf{P} , system noise covariance \mathbf{Q} , measurement noise covariance \mathbf{R} , and RANSAC threshold are equally set for fair evaluation. Besides, input feature points are also identical in all evaluations. The maximum number of feature points are set to 100 with bucketing. Estimates of rotation and translation are averaged in 10-Monte Carlo simulation. Table 1 shows that the our simple confidence incorporation leads to the quantitative performance improvement of VIO. The improvement appears in translation estimation as we intended. We can notice that the proposed algorithm really suppresses the translation error in sequence # 6, 8, 9. The qualitative comparison of these sequences are shown in Fig. 9. The rotation estimates of the proposed algorithm have negligible variation compare to the baseline. The accuracy of rotation estimates really high thanks the gyroscope measurements from the IMU though.

7 Discussion and Conclusion

In this paper, we proposed the robust VIO algorithm based on the analysis of feature confidence in ego-motion estimation using inertial measurements. We first formulate the VIO problem by using effective trifocal tensor geometry. Then, by using the motion information obtained from inertial measurements, we define the feature confidence in ego-motion estimation and propose the confidence-incorporated ego-motion estimation framework based on inertial measurements. Experimental results on the public KITTI dataset show that the proposed algorithm outperforms the baseline VIO, and it demonstrates the effectiveness of the proposed feature confidence analysis and the proposed confidence-incorporated ego-motion estimation framework.

We expect that the proposed algorithm can be applied to the smart-phone platform equipped with a low-cost IMU and a camera. Furthermore, thanks to the advances of various computer vision techniques, some other cues such as depth inferred from single image can be incorporated into our framework to extend our work.

8 References

- 1 Moravec, H.P. 'Visual mapping by a robot rover'. In: International Joint Conference on Artificial Intelligence. (, 1979).
- 2 Geiger, A., Lenz, P., Urtasun, R. 'Are we ready for autonomous driving? the kitti vision benchmark suite'. In: CVPR. (, 2012).

- 3 Laurent.Kneip, M.C., Siegwart, R. 'Robust real-time visual odometry with a single camera and an imu'. In: BMVC. (, 2011).
- 4 Hu, J.S., Chen, M.Y. 'A sliding-window visual-IMU odometer based on tri-focal tensor geometry'. In: ICRA. (, 2014).
- 5 Kaess, M., Ni, K., Dellaert, F. 'Flow separation for fast and robust stereo odometry'. In: ICRA. (, 2009).
- 6 Yang, S., Bhanu, B., Mourikis, A.I. 'Error model for scene reconstruction from motion and stereo'. In: CVPR Workshops. (, 2011).
- 7 Qian, G., Chellappa, R., Zheng, Q. 'Bayesian structure from motion using inertial information'. In: ICIP. (, 2002).
- 8 Gemeiner, P., Vincze, M. 'Motion and structure estimation from vision and inertial sensor data with high speed cmos camera'. In: ICRA. (, 2005).
- 9 Jones, E., Vedaldi, A., Soatto, S. 'Inertial structure from motion with autocalibration'. In: ICCV. (, 2007).
- 10 Huang, G.P., Mourikis, A.I., Roumeliotis, S.I. 'Observability-based rules for designing consistent EKF SLAM estimators', *IJRR*, 2010, **29**, pp. 502–528
- 11 Kneip, L., Martinelli, A., Weiss, S., Scaramuzza, D., Siegwart, R. 'Closed-form solution for absolute scale velocity determination combining inertial measurements and a single feature correspondence'. In: ICRA. (, 2011).
- 12 Dong, Si, T.C., Mourikis, A.I. 'Motion tracking with fixed-lag smoothing: Algorithm and consistency analysis'. In: ICRA. (, 2011).
- 13 Jones, E.S., Soatto, S. 'Visual-inertial navigation, mapping and localization: A scalable real-time causal approach', *IJRR*, 2011, **30**, (4), pp. 407–430
- 14 Weiss, S., Siegwart, R. 'Real-time metric state estimation for modular vision-inertial systems'. In: ICRA. (, 2011).
- 15 Lupton, T., Sukkarieh, S. 'Visual-inertial-aided navigation for high-dynamic motion in built environments without initial conditions', *TRO*, 2012, **28**, (1), pp. 61–76
- 16 PiniÁt'es, P., Lupton, T., Sukkarieh, S., TardÁt'os, J.D. 'Inertial aiding of inverse depth SLAM using a monocular camera'. In: ICRA. (, 2007).
- 17 NÁijtzi, G., Weiss, S., Scaramuzza, D., Siegwart, R. 'Fusion of IMU and vision for absolute scale estimation in monocular SLAM', *Journal of Intelligent and Robotic Systems*, 2011, **61**, (1-4), pp. 287–299
- 18 Martinielli, A. 'Vision and imu data fusion: Closed-form solutions for attitude, speed, absolute scale, and bias determination', *TRO*, 2012, **28**, (1), pp. 44–60
- 19 Dong, Si, T.C., Mourikis, A.I. 'Estimator initialization in vision-aided inertial navigation with unknown camera-imu calibration'. In: IROS. (, 2012).
- 20 Li, M., Mourikis, A.I. '3-D motion estimation and online temporal calibration for camera-imu systems'. In: ICRA. (, 2013).
- 21 Williams, B., Hudson, N., Tweddle, B., Brockers, R., Matthies, L. 'Feature and pose constrained visual aided inertial navigation for computationally constrained aerial vehicles'. In: ICRA. (, 2011).
- 22 Kottas, D.G., Roumeliotis, S.I. 'Efficient and consistent vision-aided inertial navigation using line observations'. In: ICRA. (, 2013).
- 23 Li, M., Mourikis, A.I. 'Vision-aided inertial navigation for resource-constrained systems'. In: IROS. (, 2012).
- 24 Mourikis, A.I., Roumeliotis, S.I. 'A multi-state constraint Kalman filter for vision-aided inertial navigation'. In: ICRA. (, 2007).
- 25 Dong, Si, T.C., Mourikis, A.I. 'Consistency analysis for sliding-window visual odometry'. In: ICRA. (, 2012).
- 26 Li, M., Mourikis, A.I. 'Optimization-based estimator design for vision-aided inertial navigation'. In: Proceedings of Robotics: Science and Systems. (, 2012).
- 27 Leutenegger, S., Furgale, P., Rabaudy, V., Chli, M., Konoligez, K., Siegwart, R. 'Keyframe-based visual-inertial SLAM using nonlinear optimization', *IJRR*, 2015, **34**, (3), pp. 314–334
- 28 Badino, H., Yamamoto, A., Kanade, T. 'Visual odometry by multi-frame feature integration'. In: ICCV Workshops. (, 2013).
- 29 Song, S., Chandraker, M. 'Robust scale estimation in real-time monocular sfm for autonomous driving'. In: CVPR. (, 2014).
- 30 Zhang, G., Vela, P.A. 'Good features to track for visual slam'. In: CVPR. (, 2015).
- 31 Hol, J.D., Schön, T.B., Gustafsson, F. 'Modeling and calibration of inertial and vision sensors', *IJRR*, 2010, **29**, (2), pp. 231–244
- 32 Chatfield, A.B. 'Fundamentals of high accuracy inertial navigation'. (Reston, VA. American Institute of Aeronautics and Astronautics, Inc., 1997)

[†]http://www.cvlibs.net/datasets/kitti/eval_odometry.php

Table 1 Comparison to the baseline odometry algorithm on public KITTI benchmark datasets. Rotation and translation errors are evaluated after moving 100 (m) at every frame and are averaged. The numbers in parenthesis indicate the length of the sequence which is the number of frames.

Sequence	Rotation error (10^{-2} deg/m)				Translation error (%)			
	Baseline [4]	Proposed	VISO2-M [34]	VISO2-S [34]	Baseline [4]	Proposed	VISO2-M [34]	VISO2-S [34]
#1 (481)	0.19	0.20	1.88	0.52	5.16	3.99	7.23	2.33
#2 (800)	0.86	0.86	4.89	1.81	2.58	3.37	15.16	2.89
#3 (474)	0.29	0.30	1.76	0.82	4.20	3.83	19.81	2.65
#4 (803)	0.34	0.32	2.79	1.57	3.42	2.61	11.09	1.67
#5 (395)	0.15	0.17	0.66	0.62	6.64	4.21	15.52	1.38
#6 (703)	0.31	0.30	1.32	1.34	11.67	5.38	49.70	1.97
#7 (570)	0.27	0.29	3.29	1.01	6.67	7.61	133.26	1.52
#8 (706)	0.40	0.41	2.59	1.69	13.10	4.90	236.60	2.29
#9 (729)	0.77	0.78	2.70	1.15	13.19	3.99	294.81	2.63
#10 (2380)	0.46	0.46	5.52	1.84	5.00	4.29	71.83	2.00
#11 (1104)	0.32	0.32	3.11	1.47	4.60	4.10	39.13	1.97
#12 (700)	0.42	0.41	7.77	2.49	1.69	2.02	62.91	2.21
#13 (5177)	0.54	0.53	3.33	1.86	5.94	5.56	53.75	3.94
#14 (1594)	0.38	0.37	2.62	1.50	4.86	4.40	4.55	1.84
#15 (1224)	0.41	0.41	4.72	1.44	4.76	5.24	37.34	1.22
#16 (4663)	0.46	0.46	1.98	1.20	12.79	9.76	9.58	1.48
All (23291)	0.45	0.45	3.37	1.55	7.19	5.63	52.38	2.33

33 Woodman, O.J. 'An introduction to inertial navigation'. (University of Cambridge, Computer Laboratory, 2007.

34 Geiger, A., Ziegler, J., Stiller, C. 'Stereoscan: Dense 3D reconstruction in real-time'. In: Intelligent Vehicles Symposium (IV). (, 2011.